WPJET1-CPR(17) 17071

A Pau et al.

A first analysis of JET plasma profile based indicators for disruption prediction and avoidance.

Preprint of Paper to be submitted for publication in Proceeding of
27th IEEE Symposium On Fusion Engineering (SOFE)

This work has been carried out within the framework of the EUROfusion Consortium and has received funding from the Euratom research and training programme 2014-2018 under grant agreement No 633053. The views and opinions expressed herein do not necessarily reflect those of the European Commission.

A first analysis of JET plasma profile based indicators for disruption prediction and avoidance

A. Pau[1], A. Fanni[1], B. Cannas[1], S. Carcangiu[1], G. Pisano[1], G. Sias[1], P. Sparapani[1], M. Baruzzo[2], A. Murari[2], F. Rimini[3], M. Tsalas[4], P.C. de Vries[4] and the JET Contributors[*]

EUROfusion Consortium, JET, Culham Science Centre, Abingdon, OX14 3DB, UK

[1] Electrical and Electronic Engineering Dept- University of Cagliari, Cagliari, Italy

[2] Consorzio RFX-Associazione - EURATOM ENEA per la Fusione, Padova, Italy

[3] CCFE, Culham Science Centre, OX14 3DB Abingdon, UK.

[4] ITER-Organisation, Route de Vinon sur Verdon, 13067 St Paul Lez Durance, France

Abstract

Reliable algorithms for disruption avoidance and prediction are foreseen to play a fundamental role in the JET control system for the successful operation of the machine in the upcoming DT campaigns. The integration of such algorithms is expected to be a key part also in the implementation of the ITER plasma control system. So far, most of the effort has been devoted to the prediction of disruptions, which is required to mitigate the effects of these transient events, protecting the integrity of in-vessel components. Nevertheless, to be able to put in place recover strategies or to have the possibility of a soft-landing for the plasma current, the paradigm has to be shifted to avoiding disruptions. In this work, plasma profile based indicators will be statistically analyzed showing their potential in such a perspective, where warning times and reliability of detection are crucial.

Keywords - Disruption Prediction; Disruption Avoidance; Plasma Profiles;Operational space mapping.

I. INTRODUCTION

Disruptive events still pose a serious problem for the operation of large size tokamak devices, representing, therefore, a key aspect to be considered for the design and operational strategies of next step fusion devices such as ITER and DEMO [1]. If an efficient mitigation is required to avoid damage to the machine, efficient avoidance schemes are needed to possibly bring the plasma back to a non-disruptive operating condition. The better the avoidance schemes (i.e. lower chance of a disruption), the lower the performance requirements for the mitigation schemes [2]. In this framework, disruption prediction plays a key role and in the last few years a substantial effort has been devoted to developing more sophisticated prediction systems and improving their performance both in terms of success rate and warning time [3-5]. Many of the presently developed disruption predictors mainly rely on MHD markers related to still rotating modes and, especially, to locked modes, which are basically the final precursor of most of the disruptions. Nevertheless, in many cases the warning time is still unsatisfactory with respect to avoidance requirements, and a significant step forward needs to be taken.

This work deals with the development of "plasma profile based indicators" for disruption prediction and avoidance in JET, where parameterized peaking factors have been implemented for electron temperature, density and plasma radiation profiles. Profile based indicators are important because of their close connection with the plasma stability and the destabilization of MHD modes that eventually cause the disruption. The basic interplay of the time evolution of different profiles will be described in relation to the phenomenology characterizing specific disruption types together with the relevant time scales. Furthermore, a statistical analysis aiming to describe differences and boundaries between the non-disruptive and the disruptive space as well as among specific types of disruptions will be presented, discussing the implications in terms of disruption prediction and avoidance.

II. PEAKING FACTORS

In the literature [3-6] several physics and engineering parameters have been considered both for disruption prediction and classification purposes, but many of them depend significantly on specific machine configurations or characteristics, and on the scientific program carried out throughout the experimental campaigns. As known, the performance of machine learning algorithms deteriorates outside the training domain and this poses serious concerns in terms of extrapolation to the next step fusion devices. That is why it is very important to focus the attention on something more invariant with respect to the operational domain than the engineering parameters traditionally used. For this purpose, some physics based indicators have been synthesized, which contain information on the time evolution of the main plasma profiles such as the electron temperature, the radiated power

[*] *See the author list of "Overview of the JET results in support to ITER" by X. Litaudon et al. to be published in Nuclear Fusion Special issue: overview and summary reports from the 26th Fusion Energy Conference (Kyoto, Japan, 17-22 October 2016).*

and the electron density. In fact, in many cases, the information contained in the profiles is strongly related to the phenomenology that characterizes different disruptive processes. In this paper, peaking factors, indicative of the radial profile of the aforementioned plasma parameters, have been considered as a feature to study the interaction of their time evolution during the chain of events leading to disruption.

To calculate the peaking of the profiles for the electron temperature, the ECE (Electron Cyclotron Emission) or the High Resolution Thomson Scattering diagnostics have been considered. JET ECE heterodyne radiometer consists of 96 channels over 4 data acquisition bands, allowing either first harmonic measurements (O-mode) or second harmonic measurements (X-mode). High Resolution Thomson Scattering diagnostic at JET measures electron temperature (T_e) and electron density (N_e), providing 63 data points per profile with a repetition rate of 20 light pulses per second (20Hz). The spatial resolution of the measurements for the core region and the pedestal is respectively of 1.6cm and 1cm. As the HRTS is not supposed to be available in real time for the next campaigns at JET, it has been used mainly to check the consistency of the ECE measurements and, in the few cases where ECE was not available, to replace it for the peaking factor calculation. Concerning the radiated power, the main-vessel bolometric cameras with horizontal views of the plasma cross-section (KB5H) have been used. The camera collects the radiation along 24 chords, 8 of which cross the divertor region and the region adjacent to the divertor with 8 cm separation between the chord axes. The other 16 channels cover the entire plasma (see Figure 1 left side). A simple pinhole structure is used to define the lines-of-sight of the camera [7].

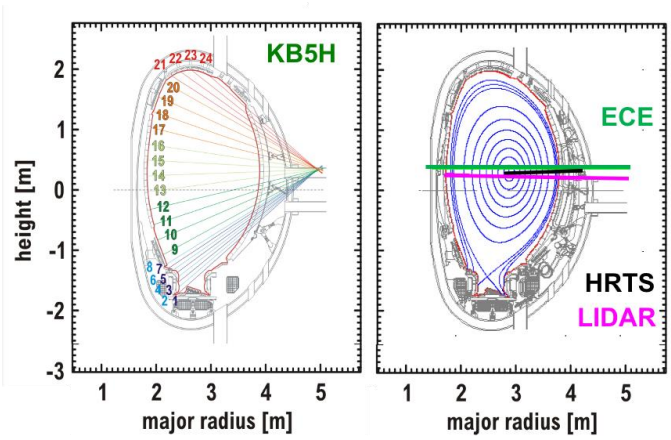

Figure 1: (left side) horizontal view bolometer KB5H at JET and (right side) line of sight in the poloidal section for ECE, HRTS and LIDAR diagnostics (right side)

Regarding the electron density profiles, the data coming from the Density Profile Reflectometry system [33-160GHz] at JET have been analyzed because of their availability in real-time. Unfortunately, because of a significant number of channels in cut-off, the coverage of the radial interval of interest turned out to be not adequate for many disruptive pulses of the considered database. Therefore, to synthesize an indicator representative of the electron density profile, again the HRTS diagnostic has been used. Another diagnostic providing kinetic profiles at JET is the LIDAR, an incoherent Thomson Scattering which measures local electron temperature and density along a horizontal almost mid-plane line of sight. With a repetition rate of 4Hz and a spatial resolution of approximately 12cm, such a diagnostic is able to provide a coverage of almost the entire plasma cross section. LIDAR data have not been used for the analyses described in this paper, but the diagnostic has been taken into account for data consistency evaluation.

Each Peaking Factor is a "core versus all" metric, i.e., it is defined as the ratio between the mean value of the considered radial profile (temperature, radiation, density) around the magnetic axis and the mean value of the measures on the entire radius. The radial interval to define the "core" has been empirically set equal to 10% of the radial axis (the minor radius for the horizontal mid-plane measurements and the vertical semi-axis of the poloidal cross section for the horizontal bolometer camera measurements). Other definitions could be adopted and different meanings could be attributed to "peaking factors" depending on the specific analysis; in this work, the aim is to define a statistically robust parameter, whose definition can be conceptually applied to the different profiles and generalized for different machines. A more detailed discussion about the implications of this definition in relation to specific physics behaviors or phenomena is out of the scope of the present paper.

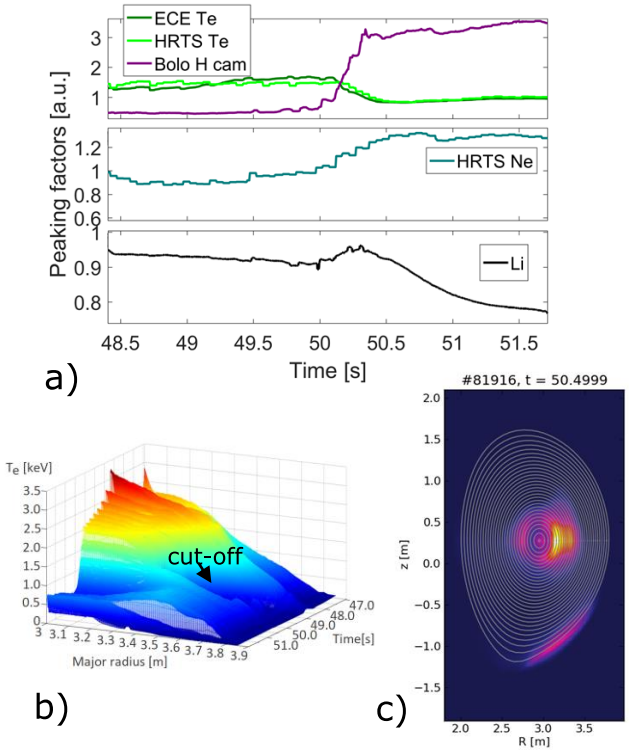

Figure 2: a) top-bottom: time evolution of the peaking factors [a.u] respectively for T_e from ECE and HRTS measurements and for the radiation from the H bolometer camera, peaking factor time evolution for the electron density (N_e) from the HRTS diagnostic, internal inductance; b) 3D spatial distribution from ECE diagnostic; c) 2D distribution of the radiation from horizontal (KB5H) and vertical bolometer cameras.

Figure 2 shows the time evolution of the radial profiles for the aforementioned plasma parameters with, in addition, the internal inductance, representative of the peaking of the plasma

current density, for a disruption due to tungsten (W) accumulation in the plasma core. In the following, we will make reference to this type of disruption characterized by core radiative collapse as *CoreRC*.

The typical process with which high-Z impurities degrade the energy confinement, leading not rarely to disruption, is well known and it has been described in several works [6]. As the sawtooth activity stops and the accumulation of W in the plasma core starts to build up, both radiation and electron density peak. On the contrary, because of the strong radiation from the plasma core (Figure 2c), the electron temperature profile flattens or even hollows depending on the plasma underlying conditions. This, in turn, gives rise to a corresponding broadening of the current density profile, as can be seen from the time evolution of the internal inductance (Figure 2a), which keeps reducing up to the final locked mode, eventually triggering the disruption. Note that the time evolution of the T_e peaking factor from the ECE diagnostic can be affected by channels in cut-off for a specific radial location, which happens for relatively high density and low field plasmas. As it is shown in Figure 2b, after ~49s a cut-off affecting the edge channels and propagating inwards translates into a slight peaking of the considered indicator. This behavior, in fact, is not in agreement with the peaking factor calculated from HRTS data, whose time evolution is roughly constant until the strong increase in the core radiation. This condition must be avoided and properly detected during real-time monitoring, and to this aim specific algorithms based on the cross-correlation of the measurements for different channels are being developed. In the database considered for this analysis, *CoreRC* disruptions represents more than the 60% of the total cases. Such disruption class is of paramount importance not only because of its strong impact on JET operations, but also because of its direct connection to the ILW (ITER Like Wall) materials.

Figure 3, conversely, shows a completely different behavior of the time evolution of the considered plasma profiles. The discharge was aimed to Pellet ELM pacing studies and a problem on the density control triggered a disruption with a MARFE developing at about 57s. The corresponding large increase of the edge density gave rise to the radiative collapse eventually degrading the plasma up to the final locked mode. This is very well described by the interplay of the peaking factors' time evolution (Figure 3a). The edge radiative collapse is synthesized by the peaking of the T_e profile, whose evolution is anticorrelated with respect to the variation of the electron density profile. It is very important to note that this behavior is building up in a condition of divertor dominated radiation and a slow progressive contraction of the plasma current profile. In the following, we will refer to this type of disruption as *EdgeRC*.

Therefore, basically, there are two components that play a role: the combination of the time evolution of the main plasma profiles and the plasma underlying conditions where the relevant phenomenology takes place. These mechanisms are strictly connected to the MHD stability, indeed, most of the time, the locked mode is the final precursor leading to disruption. Very often, the change in the profile time evolution takes place over much longer time scales, and this is extremely important for the avoidance requirements. Another third important ingredient needs to be taken into account: the robustness in the identification of boundaries and conditions leading with high probability to disruption. This aspect will be addressed in the next section describing the univariate statistical distributions of the different peaking factors.

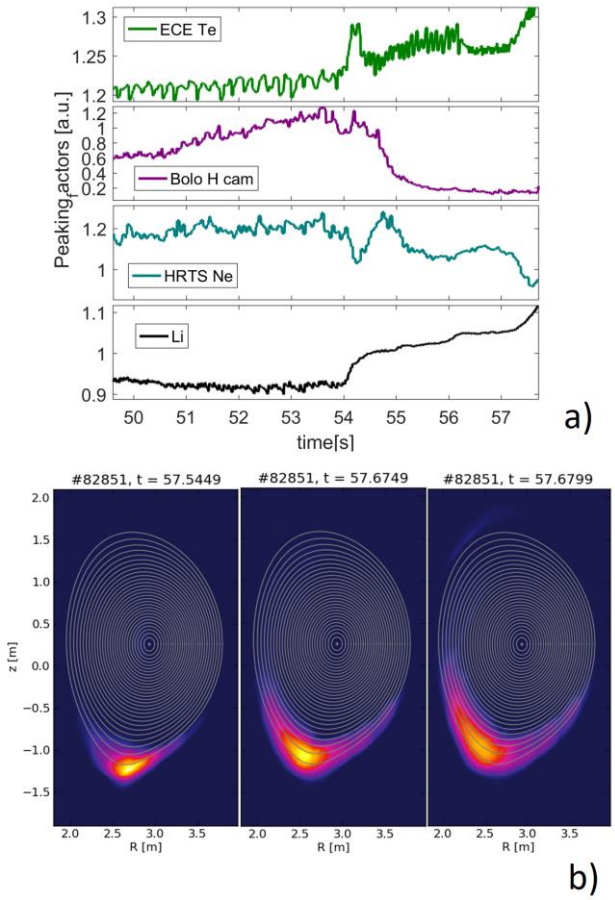

Figure 3 - Density control problem disruption; a) top-bottom: time evolution of the peaking factors [a.u] respectively for T_e from ECE, radiation from the horizontal bolometer camera, electron density (N_e) from the HRTS diagnostic, internal inductance; b) 2D distribution of the radiation from horizontal (KB5H) and vertical bolometer KB5V cameras for three different time instants showing MARFE development.

III. Univariate Statistical Analisys

A univariate statistical analysis has been performed in order to evaluate the power of each peaking factor both in discriminating between disruptive and non-disruptive behavior and among different types of disruptions. To this end, different scenarios have been considered, as described in the following of this section. Note that, in this univariate analysis, no combination among the features has been considered, which would greatly increase the discrimination and prediction capability of the plasma profiles, as will be discussed in the following section. The statistical analyses have been performed referring to a database of 149 non-intentional disruptions, already considered in other studies [6], and 126 non-disrupted pulses that occurred between 2011 and 2013. For the considered disruptions, the manual classification, already available [8-9], has been further detailed analyzing the different time intervals of the main events characterizing the disruptive

process. For a few tens of these pulses, the diagnostic signals were not available or corrupted, and consequently have been discarded. Hence the final database analyzed in this work is composed of 135 disrupted and 120 non-disrupted discharges.

A. *Disrupted versus Non Disrupted discharges*

The first scenario considers the stable phase of the disrupted discharges versus all the flat top of the non-disrupted ones, regardless of the disruption type. Hence, both classes refer to phases in which the plasma can be considered in a stable condition.

In Figure 4, the histograms of the samples coming from the flat-top of the non-disrupted pulses (blue) and from the stable phase of the disruptive pulses (red) are reported for the peaking factors of the three considered profiles, namely the electron temperature, the radiated power and the electron density, together with the internal inductance, that is itself an indicator of the peaking of the current density profile. These histograms have been normalized providing the probability density functions (pdf) and considering the same bin width for both the distributions, so that the ratio of overlapping bins gives directly the proportion in terms of probability. As can be seen, except for the electron density, the distributions are quite different. Referring, as an example, to the temperature peaking factor, the ranges of variation of the two distributions are comparable but the non-disruptive pulses have a unimodal distribution, with the maximum value corresponding to a peaking factor between 1.4 and 1.6, whereas the stable phase of the disruptive population is characterized by a bimodal distribution.

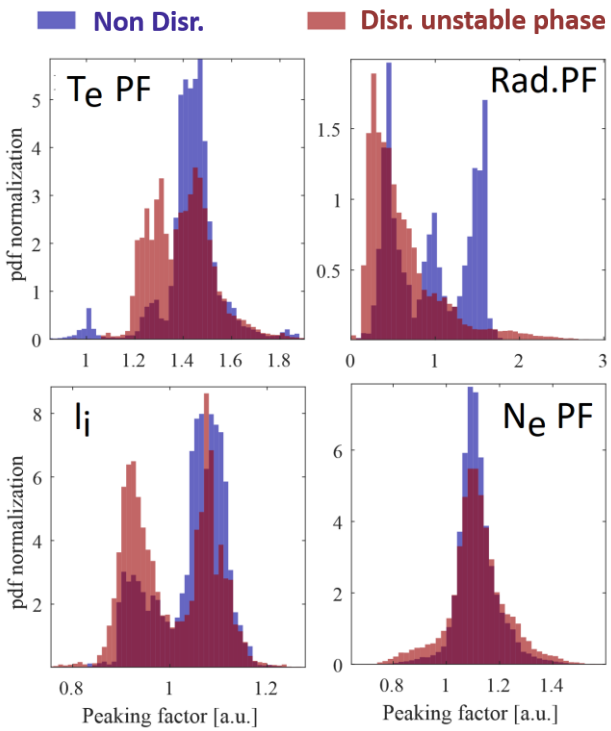

Figure 4 - Probability distribution functions of the peaking factors of the non-disruptive pulses (blue) versus the stable phase of the disruptive pulses (red) for electron temperature, radiated power, current density (internal inductance) and electron density (from top left to bottom right).

Referring to the radiation peaking, the non-disruptive discharges present a tri-modal distribution probably due to the presence, in the selected database, of a wide range of plasma scenarios and operating conditions, as expected in an experimental machine. Nevertheless, no one of the considered conditions resulted in a radiation peaking factor greater than 1.7, which can be assumed as a sort of empirical higher bound for the non-disrupted discharges.

The second scenario refers to the unstable phase of the disrupted pulses versus all the flat top of the non-disrupted shots. Figure 5 reports the probability density functions of the non-disrupted pulses (blue) and of the unstable phase of the disruptive pulses (red) for the peaking factors of the electron temperature, the radiated power, the electron density and for the internal inductance.

As can be observed, basically for all the considered parameters, the overlapping area dramatically reduced with respect to the previous analyzed scenario highlighting the potential of the introduced indicators to distinguish between disrupted and non-disrupted behaviors. In particular, the distribution of the temperature peaking factor for the phases considered for the disruptive discharges shifts towards lower values, whereas that of the radiation shifts significantly towards higher values. This, as can be easily inferred from the discussion of the examples in the previous section, is mainly due to the presence of a large percentage of *CoreRC* disruptions in the considered database, that represents one of the most common causes of disruption at JET after the installation of the ILW.

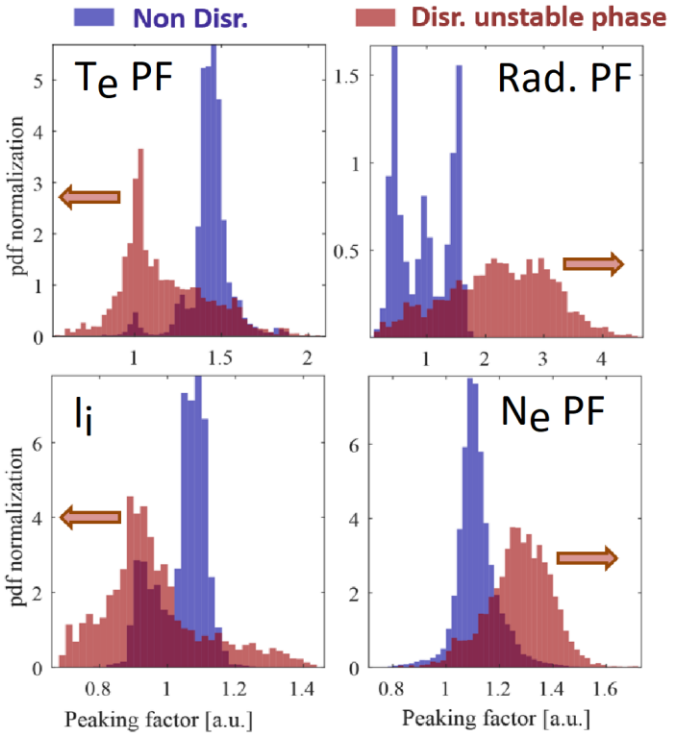

Figure 5 - Probability distribution functions of the peaking factors of the non-disruptive pulses (blue) versus the unstable phase of the disruptive pulses (red) for electron temperature, radiated power, current density (internal inductance) and electron density (from top left to bottom right).

All the distributions of the peaking factors in Figure 5 suggest the possibility to choose suitable thresholds to discriminate between disrupted and non-disrupted behaviors.

In the following, the prediction performance obtained by thresholding the radiation peaking has been shown. The prediction success rate has been evaluated in terms of missed alarms (MAs), i.e., the fraction of disruptive discharges predicted as non-disruptive, and false alarms (FAs), defined as the fraction of non-disruptive discharges predicted as disruptive.

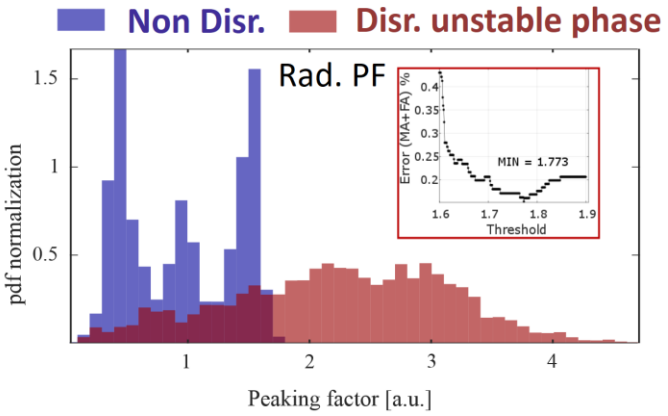

Figure 6 –Selection of the thresholds for the radiation peaking disruption predictor. In the frame, the trend of the prediction errors (MAs+FAs) with threshold.

Different thresholds have been tested. Among them, because of their intrinsic statistical meaning, that minimizing the overlapping of the two distributions according to the Bayes optimal decision boundary, which is equal to 1.59, or that corresponding to the inversion of the ratio between the two distributions, which is equal to 1.65, have been considered. Another threshold has been evaluated, minimizing the sum of MAs and FAs, which corresponds to a value of ~1.77 (Figure 6). Table I reports the prediction performance obtained with the selected thresholds.

TABLE I – PREDICTIVE PERFORMANCE OF THE KB5H PEAKING FACTOR IN TERMS OF MISSED ALARMS AND FALSE ALARMS

Threshold	Missed Alarms	False Alarms
1.59	17/135 12.59%	41/120 34.17%
1.65	18/135 13.33%	11/120 9,17%
1.77	20/135 14.81%	1/120 0.83%

As expected, the optimized threshold performs better if defined in terms of false alarms. Note that with such an optimization, among the 20 MAs, only one is due to *CoreRC* disruptions. This is due to the fact that the main phenomenology characterizing this disruption type is exhaustively described by the time evolution of the considered profile and that the defined peaking factor results to be robust enough to catch the changes involved in the unstable phase leading to disruption. On the other hand, the larger variety of behaviors characterizing the disruption classes collected in the other group (*EdgeRC*) involves a broader plethora of phenomena where the time evolution of the considered profiles combines in different ways. Hence, it is worth performing a further univariate analysis discriminating between *CoreRC* and *EdgeRC* disruptions.

B. *CoreRC versus EdgeRC disruptions*

The univariate analysis performed on the previously calculated peaking factors, resulted to be useful also to have a first discrimination among different types of disruptions. In fact, the information contained in the profiles is connected to the phenomenology characterizing different disruptive processes. Figure 7 reports the probability density functions of the unstable phase of the high-Z impurity accumulation disruptions (*CoreRC*) (purple) and that of the unstable phase of all the other disruptions (*EdgeRC*) (green) for the peaking factors of the electron temperature, the radiated power, the electron density and for the internal inductance.

As in the previous cases, the probability density functions of the different peaking factors are quite different comparing the *CoreRC* disruptions versus all the *EdgeRC* disruptions. In particular, in the unstable phase, *CoreRC* disruptions present values of the temperature peaking factor significantly lower than that of the other disruptions. This is consistent with the phenomenology that characterizes the *CoreRC* class, namely flattening or even hollowing of the radial temperature profile.

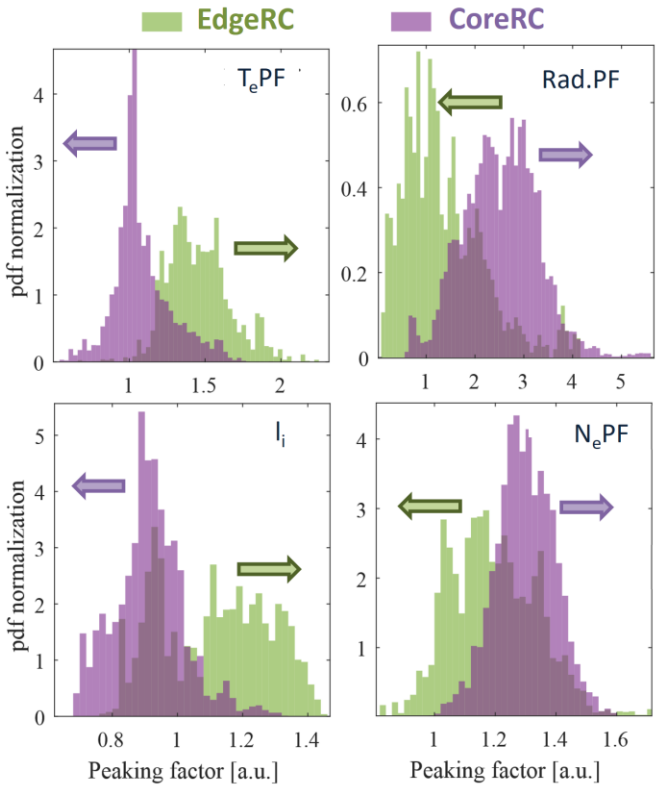

Figure 7 - Probability distribution functions of the peaking factors of the unstable phase of the *CoreRC* disruptions (purple) versus the unstable phase of the *EdgeRC* disruptions (green) of electron temperature, radiated power, internal inductance and electron density (from top left to bottom right).

Conversely, the peaking factors related to the unstable phase of *EdgeRC* disruptions have a statistical distribution

driven by the cooling radiative collapse at the edge, which is a common feature of the final path of the disruptions grouped in this class.

The unfolding of such a phenomenology, as well known, involves the contraction/peaking of the electron temperature and current density profiles, and, on the other hand, a strong increase of radiation and density at the edge, that reflects in a shift of the distributions towards lower values of the respective peaking factors. Also in this case, suitable thresholds could be optimized to discriminate among different classes. However, as discussed in the initial section, what is really powerful is the information associated to the interplay of the individual profiles, and this will be discussed in the next section in terms of multidimensional space analysis.

C. Warning Times

The characterization of the *CoreRC* versus the *EdgeRC* disruptions keeps being quite different also considering the warning times obtained by thresholding the single peaking factors. As an example, Figure 8 reports the distributions of the expected warning time, evaluated with respect to the start of the chain of events leading to disruption (Figure 8 top), and of the actual warning time obtained by simply thresholding the radiation peaking factor (Figure 8 bottom) for the two analyzed disruptive groups.

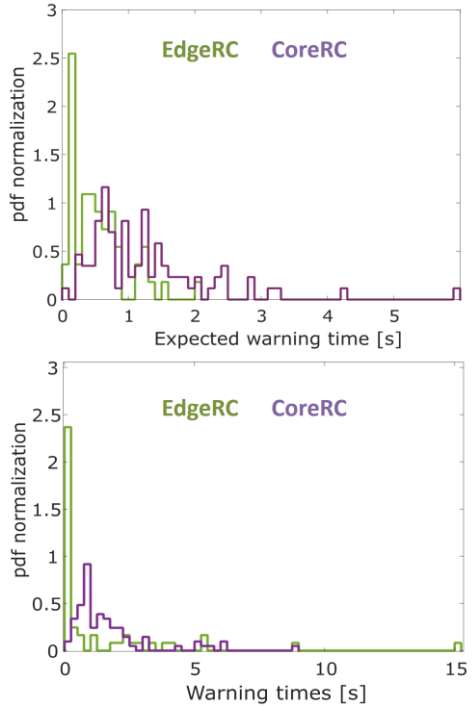

Figure 8 - Probability density functions of the warning times of *CoreRC* (purple) vs *EdgeRC* (green) disruptions. Top: Expected warning times evaluated with respect to the start of the chain of events leading to disruption; Bottom: actual warning times obtained thresholding the radiation peaking factor (note that in this case, the threshold obtained by minimizing the sum of MAs and FAs gives rise also to some early detection, associated to warning times higher than those expected and not directly connected to the chain of events leading to disruption).

As can be seen, by comparing these latter with the expected ones, the warning time distributions are qualitatively similar, especially for the *CoreRC* disruptions, and confirm the potential of the proposed indicators for avoidance purposes.

IV. Machine Learning for the Multidimensional Analysis

As well known, disruptions can be due to the non-linear interaction of many parameters and, depending on the causes and the phenomenology, they can evolve in different regions of the operational space. In the very recent last years, one among the most advanced machine learning techniques has been successfully exploited to investigate the JET high-dimensional space where the relevant disruption physics takes place [5-6]. Such a technique, that is the Generative Topographic Mapping (GTM), is a generative model that belongs to the class of the so called manifold learning techniques. By mapping on a low dimensional space the complex manifold embedded in the high dimensional space, the GTM algorithm allows uncovering complex structures, patterns and operational boundaries described by the complex relation among the parameters in the considered operational space. The technique performs a non-linear mapping through Radial Basis Functions (RBF) from the latent space to the data space, fitting a mixture of Gaussians which are constrained to lie on the low dimensional space embedded in the original high dimensional one. Despite the complexity of the model, the concept behind the method is very simple: since the mapping is defined by a smooth and continuous non-linear function, the topographic ordering and the proximity relations in the latent space are preserved in the original data space, regardless of the dimensionality reduction. In fact, for visualization purposes, the latent space is chosen to be 2 or 3 dimensional [10]. Figure 9 reports the GTM scheme for the mapping from the latent space to the data space.

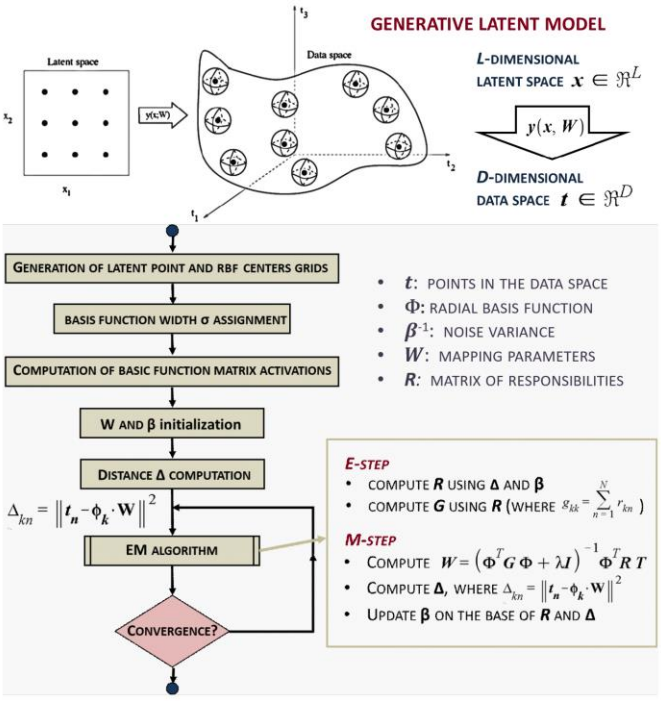

Figure 9 - GTM mapping. Top: the correspondences between a data point in the manifold embedded in the data space and the mean of the posterior distribution in the latent space; Bottom: GTM calculation workflow.

In this work, the GTM tool developed in [11] has been exploited to map a 5-dimensional space including only indicators representative of the radial profiles described in the previous sections, namely:

- T_e profile Peaking factor from ECE diagnostic
- Radiation profile Peaking factor from the horizontal bolometer camera
- Internal inductance Li (current density profile Peaking factor) from EFIT equilibrium code
- q_{95}/q_0 ratio from EFIT equilibrium code
- N_e profile Peaking factor from HRTS diagnostic

To the set of 4 parameters already discussed in the previous sections, the q_{95}/q_0 ratio has been added to investigate possible differences with respect to the information provided by the internal inductance. In Figure 10, the pie-plane representation of the resulting 2-dimensional GTM mapping is shown. Such a mapping has been obtained for a latent square grid of 45x45 points, 196 RBF with a width σ of 1.5. Such parameters have been chosen to guarantee a good tradeoff between smoothness and flexibility of the non-linear mapping for the considered dataset, which consists of about 110000 samples for each feature in input. What is particularly interesting to observe is the quite well-defined separation among the three considered classes in the analyzed parameter space.

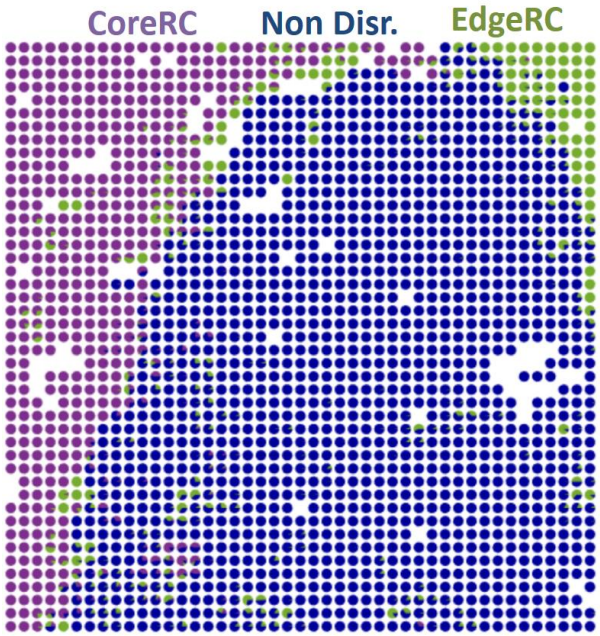

Figure 10 - GTM pie-plane of posterior probability modes: the non-disruptive samples are represented in blue, the samples coming from *EdgeRC* disruption in light green and the samples coming from *CoreRC* disruptions.

In particular, it is possible to define a boundary separating the region of the operational space dominated by the non-disruptive samples from the regions occupied by the two disruptive classes, where the *EdgeRC* is located mostly in the upper right corner, whereas the *CoreRC* class occupies entirely the left side with a broadening in the upper part of the map. Whilst the distribution on the map of the *CoreRC* class is quite smooth, giving rise to a large, almost continuous area, the *EdgeRC* distribution is characterized by a slightly larger spread on the map, which can be explained by the significant heterogeneity of the disruption phenomenology composing the *EdgeRC* group itself.

Another powerful way to visualize data, implemented in the GTM tool previously mentioned, is represented by the component planes analysis, with which it is possible to study characteristic patterns and structures hidden in the high dimensional data by analyzing the relative component distribution of the input parameters associated to the 2D mapping.

In Figure 11, the component planes for all the input parameters have been reported. As can be seen, the distribution of the input parameters shows up all the main features already discussed in the section dedicated to the univariate analysis, highlighting the combination of the input parameters that provide the separation among the considered classes in the 2-dimensional space.

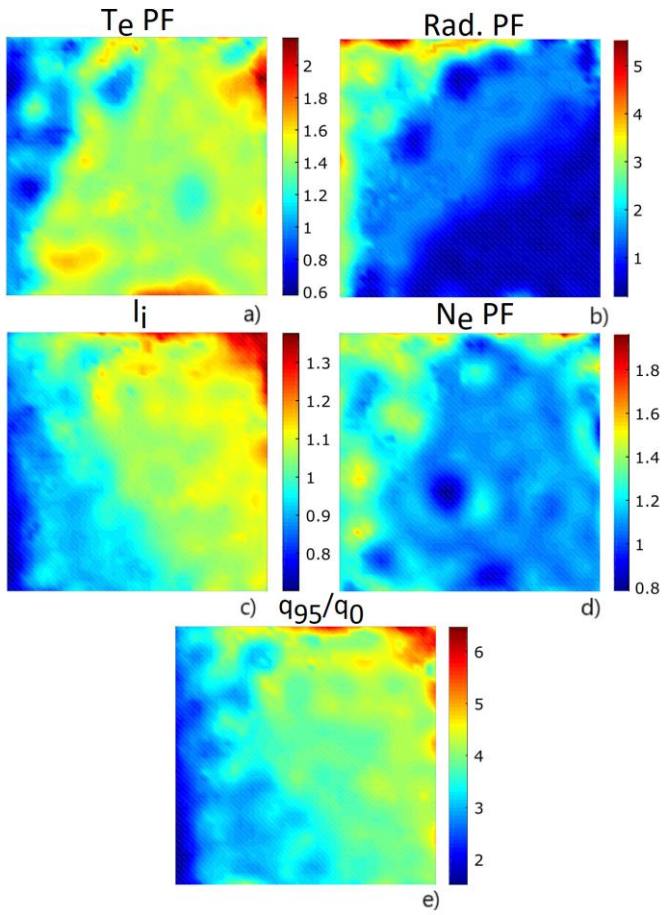

Figure 11 - GTM Component Planes of the of electron temperature peaking factor (T_ePF), radiation peaking factor (Rad.PF), internal inductance (l_i), electron density peaking factor (N_ePF), and safety factor ratio (q_{95}/q_0).

Moreover, it is interesting to note that, as expected, the distribution of the internal inductance resembles the q_{95}/q_0 ratio distribution, since they are both strictly related to the peaking of the current density profile. We can also observe that the

smoothest distributions are related to the radiation peaking factor and again to the internal inductance (or the q_{95}/q_0 ratio), where the gradient of the distribution itself changes almost linearly along the diagonal direction (bottom-right corner to upper-left corner for the radiation peaking, bottom-left corner to upper-right corner for the internal inductance). This is an indication of a lower complexity as far as the contribution of these two parameters to the mapping is concerned. On the contrary, the distribution on the identified manifold for the T_e and N_e profiles peaking factors is characterized by a more structured behavior that could be attributed to a not straightforward combination of the considered parameters for specific cases included in the dataset. Technically, they depend on the direction of stretching or compression of the 2-D manifold embedded in the 5-D space, that is required to fit the data.

V. Conclusions and Future works

In this work, peaking factors for the main plasma profiles have been defined for the JET tokamak with the aim of extracting the information carried out by their evolution in time, and have been statistically analyzed for a database with the ILW. The main profiles considered for the analysis are related to the electron temperature (T_e), the electron density (N_e), the radiation, the ratio q_{95}/q_0, and finally the internal inductance, intrinsically indicative of the peaking of the plasma current profile itself. Each peaking factor is a "core versus all" metric, i.e., it has been defined as the ratio between the mean value of the considered radial profile around the magnetic axis and the mean value of the measures on the entire radius. The radial interval to define the "core" has been empirically defined as 10% of the radial axis.

Different scenarios have been analyzed discriminating the non-disruptive discharges from the disruptive ones, and identifying among this latter two main groups: high-Z impurity accumulation disruptions, labeled as *CoreRC*, and disruptions characterized by a final edge radiative cooling (already analyzed in [5]), labeled as *EdgeRC*. These plasma profile based indicators have been firstly analyzed by performing a univariate statistical analysis, already showing their high potential in discriminating among the considered classes.

After that, the interplay of the time evolution of the different profiles has been analyzed combining all the features with an advanced manifold learning algorithm, the Generative Topographic Mapping (GTM), highlighting a quite well-defined separation among the classes object of the study in the considered parameter space. This result, together with the expected warning times that came out from the analysis, is very promising in the perspective of avoiding and predicting disruptions, which is crucial for JET operations in the upcoming DT campaigns as well as for the design of the ITER Plasma Control System.

Future work will regard an optimization and a more refined analysis of the defined physics based parameters, with particular reference to diagnostic data available in real-time, and an extension of the analysis to larger databases including further ILW campaigns.

Finally, the exploitation of other machine learning techniques to cooperate with GTM, such as the Random Forests [11], has recently started, showing a huge potential for the application in the prediction and the avoidance of disruptions. In this perspective, the compatibility and the possible integration in the JET real-time control system will be the object of further investigations in the very near future.

ACKNOWLEDGMENT

This work has been carried out within the framework of the EUROfusion Consortium and has received funding from the Euratom research and training programme 2014-2018 under grant agreement No 633053. The views and opinions expressed herein do not necessarily reflect those of the European Commission or the ITER Organization.

References

[1] Wesson, J. Tokamaks 2rd edn, Ch. 3, 105–138 (Oxford Univ. Press, Oxford, 1997.

[2] [2] P.C. de Vries, et al., Requirements for triggering the ITER Disruption Mitigation System, Fusion Science and Technology 69 (2016) 471

[3] B. Cannas, A. Fanni, P. Sonato, M.K. Zedda and EFDA-JET contributors, "A prediction tool for real-time application in the disruption protection system at JET," *Nuclear Fusion*, vol. 47, pp. 1559–1169, 2007.

[4] G.A. Rattá, J. Vega, A. Murari, G. Vagliasindi, M.F. Johnson, P.C. de Vries, and EFDA-JET Contributors, "An advanced disruption predictor for JET tested in a simulated real-time environment," Nuclear Fusion, vol. 50, 025005 (pp.10), 2010.

[5] B. Cannas, A. Fanni, A. Murari, A. Pau, G. Sias, and JET EFDA Contributors, "Overview of manifold learning techniques for the investigation of disruptions on JET", *Plasma Physics and Controlled Fusion* , vol. 56, 2014.

[6] B. Cannas, P.C. de Vries, A Fanni, A Murari, A Pau, G Sias, and JET EFDA Contributors, "Automatic disruption classification in JET with the ITER-Like Wall", *Plasma Physics and Controlled Fusion*, vol. 57, 2015.

[7] A. Huber, et al., "Upgraded bolometer system on JET for improved radiation measurements", *Fusion Engineering and Design*, Vol, 82, pp. 1327–1334, 2007.

[8] P C de Vries, et al., "The influence of an ITER-like wall on disruptions at JET", *Physics of Plasmas*, vol. 21, 056101, 2014.

[9] P.C. de Vries, M.F. Johnson, B. Alper, P. Buratti, T.C. Hender, H.R. Koslowski, V. Riccardo, and JET-EFDA Contributors, "Survey of disruption causes at JET", *Nucl. Fusion*, vol. 51, 053018 (12pp), 2011.

[9] Bishop C., Svensén M., Williams C. (1998) GTM: The generative topographic mapping Neural Computation 10 215–34.

[10] A. Pau, "Techniques for prediction of disruptions on TOKAMAKS". [Ph.D Thesis], http://paduaresearch.cab.unipd.it/6664/, 2014.

[11] L. Breiman, "Random Forest", Machine Learning, 45, 5-32, 2001.